ORIGINAL ARTICLE

A semiconducting molecular ferroelectric with a bandgap much lower than that of BiFeO$_3$

Peng-Fei Li[1], Yuan-Yuan Tang[1], Wei-Qiang Liao[1], Heng-Yun Ye, Yi Zhang, Da-Wei Fu, Yu-Meng You and Ren-Gen Xiong

Ferroelectrics have been attracting increasing attention as good candidates for multifunctional materials because of their fascinating properties. However, their large bandgap has been a roadblock limiting their application in optoelectronics and photovoltaics, among other applications. Hybrid ferroelectrics have the potential to combine the advantages of both molecular materials and ferroelectrics. In this context, we designed a hybrid ferroelectric: (2-(ammoniomethyl)pyridinium)SbI$_5$. It shows an above-room-temperature Curie temperature ($T_c = 360$ K), a large spontaneous polarization ($P_s = 4$ μC cm^{-2}) and a small bandgap (2.03 eV) that is much smaller than the recently reported 2.7–3.65 eV for the lead-halide perovskite ferroelectrics. The implementation of ferroelectricity in hybrid semiconducting materials may be a feasible way to realize high-performance ferroelectric optoelectronic and photovoltaic devices.

INTRODUCTION

Intensive research on photovoltaic (PV) materials over the past six decades has been driven by the increasingly serious energy crisis. Among the emerging PV technologies, hybrid perovskite solar cells demonstrate extraordinary power conversion efficiencies and very low cost.[1–5] The high power conversion efficiency (up to 20.1%) is because of the strong light absorption and high carrier mobility of hybrid perovskites. Nevertheless, much work needs to be done to overcome their instability in moisture and the toxicity of lead. Thus, researchers have begun to explore related materials with a lower toxicity and/or better stability.[6–8]

Meanwhile, the past few years have seen the renaissance of photoferroelectric materials for PV applications.[9–12] Photoferroelectric materials, such as BiFeO$_3$ and SbSI, are semiconducting ferroelectrics that show both photosensitive and ferroelectric properties. They adopt a newly described mechanism known as the anomalous PV effect, where photogenerated electrons and holes are directly separated by the spontaneous electric field from the intrinsic ferroelectric polarization, resulting in an open circuit voltage above the bandgap. However, the power conversion efficiency of conventional inorganic ferroelectrics remains low because of the poor light absorption ability that is limited by their large bandgaps.

Organic–inorganic hybrid ferroelectrics have the potential to combine advantages from both hybrid materials and ferroelectrics. We recently demonstrated that photoferroelectricity can be achieved in lead-halide perovskite-type ferroelectrics.[13,14] Although these compounds show excellent ferroelectricity, they have two drawbacks: a relatively high bandgap (> 2.7 eV) and toxicity from the Pb element.

Therefore, environmentally friendly hybrid ferroelectrics with a smaller bandgap are highly desirable. Inspired by the recently discovered PV effect in hybrid perovskites A$_3$Bi$_2$I$_9$ (A: methylammonium or cesium),[15,16] we have synthesized a hybrid semiconducting ferroelectric (2-(ammoniomethyl)pyridinium)SbI$_5$ (1). This material shows a narrow bandgap of 2.03 eV, comparable to that for SbSI ($E_g = 2.0$ eV) and much lower than that for BiFeO$_3$ ($E_g = 2.7$ eV), that may be suitable for PV applications. Herein we report the semiconducting, ferroelectric and related properties of 1.

MATERIALS AND METHODS

Synthesis

Sb$_2$O$_3$ (5.0 mmol, 1.45 g) was dissolved in HI solution (45%, 100 ml). Thereafter, 2-(ammoniomethyl)pyridine (10.0 mmol, 1.08 g) was added dropwise, and the precipitate was dissolved by refluxing at 373 K. Large, dark-red crystals of 1 were obtained by slowly cooling the clear solution at the rate of 1 °C/6 h. The purity of the bulk phase was verified by powder X-ray diffraction (Supplementary Figure S1). CCDC 1435416-1435418 contain the supplementary crystallographic data for this paper. These data can be obtained free of charge from The Cambridge Crystallographic Data Center at www.ccdc.cam.ac.uk/data_request/cif.

Methods

Methods used for differential scanning calorimetry, second harmonic generation (SHG), dielectric measurement, pyroelectric measurement and measurement of P–E hysteresis loops have been described elsewhere.[17,18] For dielectric and P–E hysteresis loop measurements, single-crystal plates ~ 5 mm^2 in area and 0.5 mm in thickness were cut from the large crystals in the [0 1 0]

Ordered Matter Science Research Center, Southeast University, Nanjing, People's Republic of China
[1]These authors contributed equally to this work.
Correspondence: Dr H-Y Ye or Professor R-G Xiong, Ordered Matter Science Research Center, Southeast University, Nanjing 211189, People's Republic of China.
E-mail: hyye@seu.edu.cn or xiongrg@seu.edu.cn

direction. Silver conducting paste deposited on the plate surfaces was used as the electrodes.

Absorption spectrum

Ultraviolet–visible (UV–vis) diffuse reflectance (transmission for thin film) spectroscopy measurements were performed at room temperature using a Shimadzu (Tokyo, Japan) UV-2600 spectrophotometer with an ISR-2600Plus integrating sphere operating from 200 to 1000 nm. $BaSO_4$ was used as the 100% reflectance reference. Powdered crystals of **1** were prepared for the measurements. The generated UV–vis spectra were used to estimate the bandgap of the material by converting reflectance data to absorbance according to the Kubelka−Munk equation: $F(R_\infty) = (1 - R_\infty)^2 / 2R_\infty$. The optical bandgap was determined from the variant of the *Tauc* equation:

$$(h\nu \cdot F(R_\infty))^{1/n} = A(h\nu - E_g)$$

where h is Planck's constant, ν is the frequency of vibration, $F(R_\infty)$ is the Kubelka−Munk equation, E_g is the bandgap and A is a proportional constant. The value of the exponent n denotes the nature of the optical transition. For direct transition, $n = 1/2$; for indirect transition, $n = 2$. Hence, the optical bandgap E_g can be obtained from a *Tauc* plot by plotting $(h\nu \cdot F(R_\infty))^{1/n}$.

Theoretical calculation

Density functional theory was adopted to investigate the electronic properties of **1** using the CASTEP module[19] coded in the Materials Studio software (Accelrys, San Diego, CA, USA). The generalized gradient approximation of the Perdew–Burke–Ernzerhof functional form[20] was used to describe the exchange and correlation interaction. The norm-conserving pseudopotential was applied in these calculations. The valence electrons of the component elements were treated as Sb $5s^25p^3$, I $5s^25p^5$, N $2s^22p^3$, C $2s^22p^2$ and H $1s^1$. First, geometrical optimization was performed by fixing the lattice constant based on the experimental X-ray crystal structure. The plane wave cutoff energy and the convergence threshold of total energy were set to 820 eV and 10^{-5} eV per atom, respectively. Then, the electronic band structures and the density of states were calculated for the optimized geometry. The self-consistent convergence of the total energy was set as 10^{-6} eV per atom.

Thin film fabrication

Ferroelectric thin films of **1** were grown by the spin-coating method. To be specific, 500 mg crystals of **1** was dissolved in 0.6 ml *N,N*-Dimethylformamide to give a clear precursor solution. For the UV–vis transmission spectrum test, 40 µl solution was spin-coated on a quartz substrate at 6000 r.p.m. for 40 s, and then the film was annealed at 120 °C for 5 min to remove the solvent and further improve the crystallinity. For piezoresponse force microscopy tests, 20 µl of solution was spin-coated on an indium tin oxide-coated glass substrate and then annealed at 120 °C for 5 min.

RESULTS AND DISCUSSION

Compound **1** can be easily synthesized in the form of single crystals from the aqueous solution of HI. It shows much better moisture stability than the currently intensively studied hybrid lead-halide layered perovskites. The film is stable when exposed to air for a few days. The thermal stability is up to 500 K (Supplementary Figure S2, Supplementary Information). Therefore, **1** has better moisture stability and lower toxicity compared with the hybrid lead-halide perovskites.

A crystal of **1** consists of infinite zig-zag perovskite chains of corner-shared SbI_6 octahedra along the *b*-axis and discrete 2-(ammonio-methyl)pyridinium cations. Zig-zag chains of octahedra have previously been observed for Sn(II), Pb(II), Sb(III) and Bi(III) compounds.[21] The neighboring chains along the *c*-axis adopt an eclipsed conformation separated by organic cations that is understood to be a pseudo (110)-oriented monolayer of the three-dimensional perovskite structure, as described in detail by Mitzi and colleagues[22,23] (Figures 1a and b). This inorganic part of the hybrid perovskite structure is responsible for their interesting electronic and optical
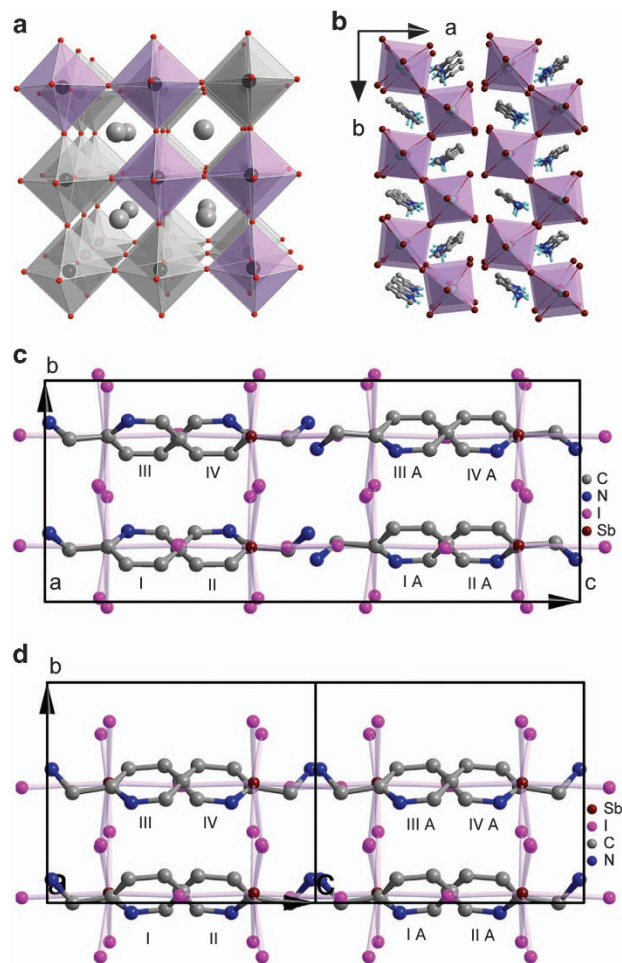
Figure 1 Comparison of the crystal structures of the paraelectric and ferroelectric phases of **1**. (**a**) The three-dimensional structure of $BaTiO_3$. A zig-zag chain is shown in purple. (**b**) A packing view of **1**, showing the one-dimensional structure. (**c**) A projection of the crystal structure at 403 K along the *a*-axis. The red dashed lines indicate the *c*-glides. (**d**) A projection of the crystal structure at 293 K along the *a*-axis. Hydrogen atoms were omitted for clarity.

properties.[24–28] At room temperature, the crystal structure has the polar space group $Pb2_1a$ (for crystallographic information, see Supplementary Data 1).

To satisfy the symmetry requirement for a ferroelectric, there should be a centrosymmetric phase at a high temperature.[29] We examined the structural phase transition by thermal analysis and found two sequential phase transitions at around $T_{c1} = 360$ K and $T_{c2} = 390$ K (Supplementary Figure S3). For convenience, we label the phase below T_{c1} as the low-temperature phase (LTP), the phase between T_{c1} and T_{c2} as the intermediate-temperature phase (ITP) and the phase above T_{c2} as the high-temperature phase (HTP).

The ITP and HTP have the same space group $Pbca$, but the unit cell volume of the ITP is double that of the HTP (for crystallographic information, see Supplementary Data 2 and 3). The volume doubling is because of the orientational changes of the organic cations produced by rotating the ammonium heads and/or the pyridinium rings along the C–C single bonds (Supplementary Figures S4 and S5, Supplementary Information). Here, we compare the LTP and HTP to determine the structural similarities and differences to understand the ferroelectric mechanism. As shown in Figures 1c and d and

Supplementary Figure S6 (Supplementary Information), the obvious differences are the changes in the orientations of the ammonium heads and the pyridinium rings. In a unit cell of the HTP (Figure 1c), there are four groups of cations (the cations numbered with I and IA are a group, and so on), and each group contains two organic cations that are related by the c-glides in the [0 1 0] direction. Accordingly, the two organic cations in the same group have different orientations, and their polarities cancel each other in the [0 1 0] direction. The LTP is derived from the HTP by rotating the ammonium heads and/or the pyridinium rings along the C–C single bonds. In the LTP, the glide symmetry is lost. The two cations in the same group are related by translation along the c-axis and thus have the same orientation. As shown in Figure 1d, all cations are aligned along the b-axis that should lead to polarization along the b-axis. The (ammoniomethyl)pyridinium cation has a structure similar to that of the benzylammonium cation, and the same rotation in the phase transition has been observed.[14] Therefore, the alignment of the organic cations is responsible for the ferroelectricity in 1. This is different from that in the three-dimensional methylammonium lead-halide perovskites. The methylammonium cations in the methylammonium lead-halide perovskites are dynamically disordered at room temperature,[30] and the observed hysteresis behavior in the current–voltage curves was recently proved to be due to ion conduction.[31,32] The formation of the same orientation for the two cations in the LTP leads to a displacement of 0.2139 Å of the positive charges that are carried by the protonated N atoms that can induce a polarization of 4 µC cm^{-2} and are comparable to the experimental value (see below).

The symmetry change was verified by the SHG measurement, a powerful method for testing crystalline materials for the absence of a center of symmetry. The LTP shows a strong SHG response (Figure 2a) that is consistent with the assignment of the polar space group. The SHG signal vanished at around T_{c1}, indicating that both the ITP and HTP are centrosymmetric. The spatial symmetry change between the paraelectric and ferroelectric phases is illustrated in Supplementary Figure S7, Supplementary Information.

In contrast to the SHG response, the dielectric response shows two sequential anomalous increases during heating (Figure 2b). Both anomalous increases are significant because the transitions involve reorientations of the dipole moments of the organic cations. Such dielectric behavior has also been observed for transitions involving rotations of organic cations in other molecular compounds.[33] The step-like increases indicate the discontinuous nature of the first-order transitions.

To demonstrate the switchable polarization nature (ferroelectricity), P–E hysteresis loops were obtained.[29] The loops were recorded at temperatures above 338 K using a Sawyer-Tower circuit,[34] with an electric field parallel to the b-axis. As shown in Figure 2c, at 363 K, above T_{c1}, a flat loop was observed showing the typical behavior for a paraelectric phase, and the minor hysteresis is due to current leakage. However, at temperatures below T_{c1}, rectangular loops were observed, providing evidence for switchable polarization. The saturated polarization (P_s) at 338 K is ~ 4.0 µC cm^{-2}, and this is among the highest values that can be observed for molecular ferroelectrics.[17,35–41] This result is consistent with the value obtained by integrating the pyroelectric current (Figure 2d). To minimize the effect of leakage current, P_s was also measured by the double-wave method[42] at room temperature, and similar results were obtained (Supplementary Figure S8, Supplementary Information).

To visualize the polarization switching behavior, we employed piezoresponse force microscopy that allows imaging, manipulation and quantitative analysis of local domain structures and the polarization properties on the sample surface. The piezoresponse force
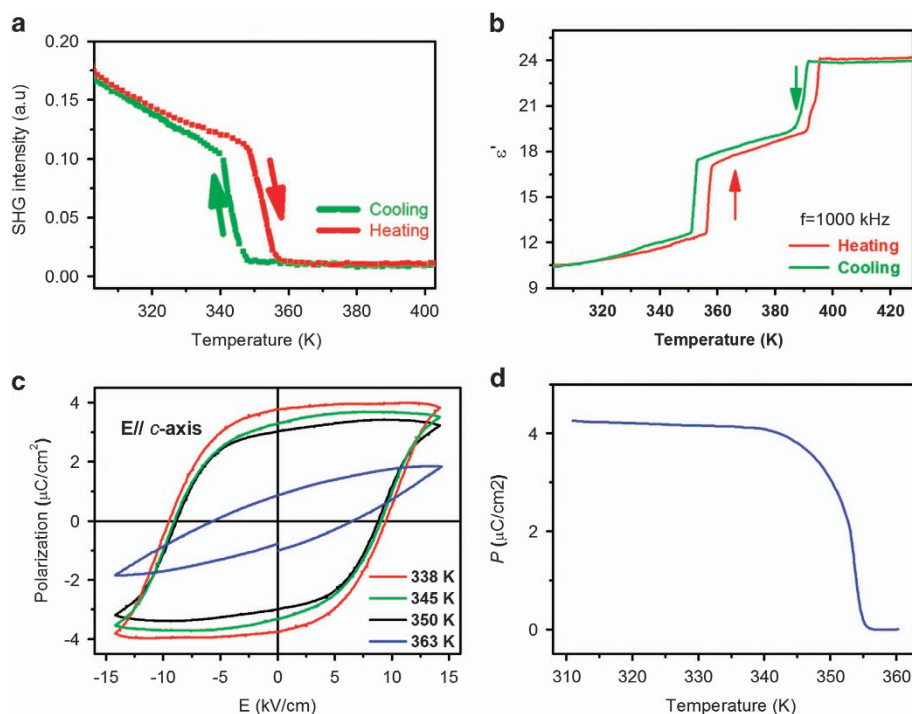
Figure 2 Ferroelectric and related properties in 1. (a) The temperature-dependent second harmonic generation (SHG) signal, showing only one transition from a polar phase to a centrosymmetric phase. (b) The temperature dependence of the real part of the complex dielectric constant ($\varepsilon = \varepsilon' - i\varepsilon''$, where ε' is the real part and ε'' is the imaginary part) at 1 MHz. (c) P–E hysteresis loops at various temperatures recorded on a Sawyer-Tower circuit. (d) The spontaneous polarization calculated by the integration of the pyroelectric current.
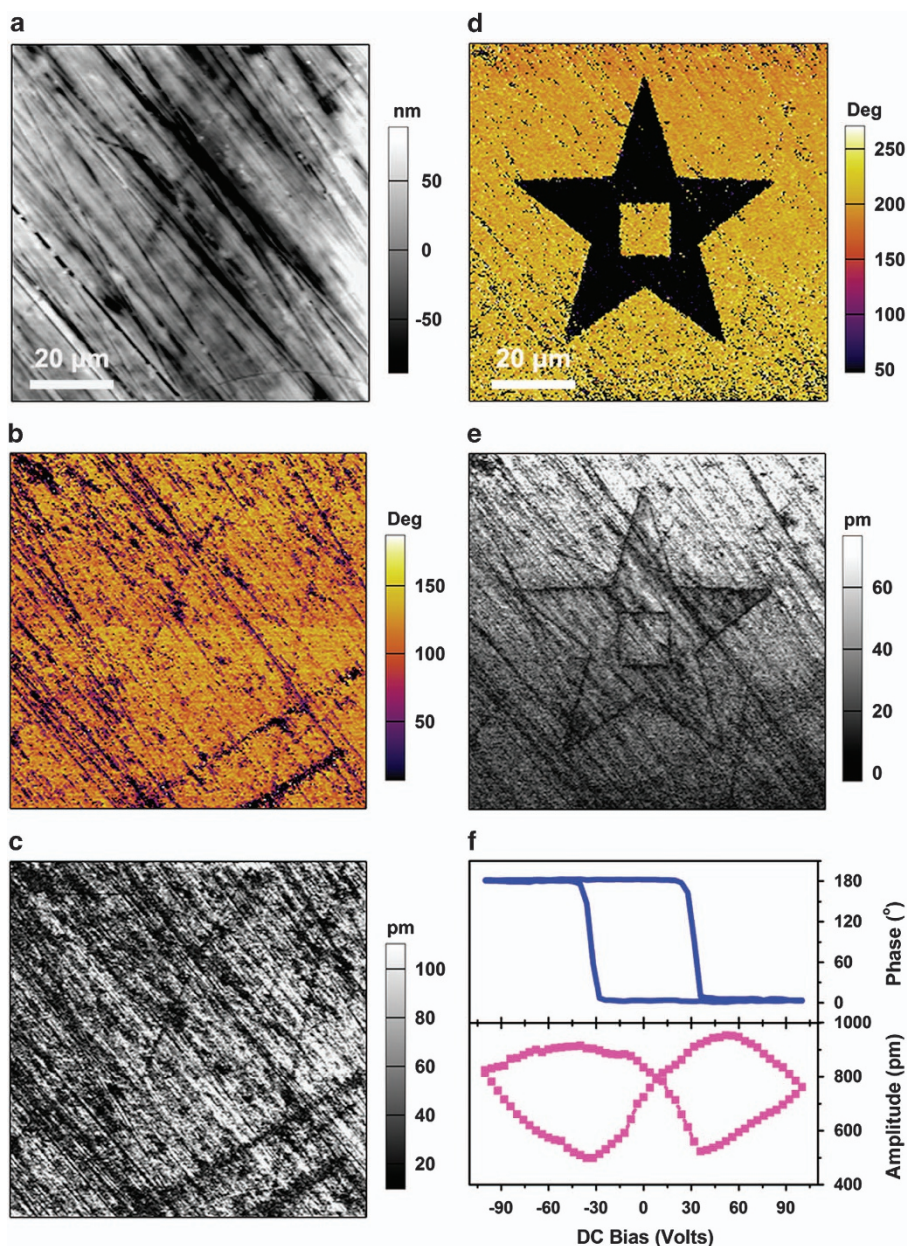
Figure 3 Polarization switching properties of **1** investigated by piezoresponse force microscopy (PFM) imaging. (**a–c**) Images constructed by surface morphology, phase and amplitude of the crystal surface, respectively. (**d**, **e**) Domain manipulation by directly switching the domain direction with various tip voltages at certain areas. The yellow and dark colors in the phase image indicate the regions in which the polarization is orientated upward and downward, respectively. (**f**) PFM spectroscopy showing the phase and amplitude signals as functions of the tip voltage.

microscopy image can be characterized by the amplitude and phase parameters that provide information about the magnitude and orientation of the polarization, respectively. Figures 3a–c show the single-domain structure of the thin plate cut from an as-grow crystal of **1** in the [0 1 0] direction. To demonstrate the manipulation of the domain structure and polarization direction, we 'drew' a star on the surface of the sample with a tip voltage of $T_{ip} = -50$ V that flips the local polarization downward, and then drew a rectangle at the center of the star with a tip voltage of $T_{ip} = 50$ V that flips the polarization direction upward. The obtained multidomain structure reveals the switchability of the spontaneous polarization (Figures 3d and e). The switchability was also recorded as the field dependencies of the phase and amplitude (Figure 3f). The phase–field hysteresis loop

and the amplitude–field butterfly curve are typical for a ferroelectric. In addition to the bulk sample, we also tested the polycrystalline thin film sample with the piezoresponse force microscopy method. The results parallel those for the bulk single crystal (Supplementary Figures S9 and S10, Supplementary Information).

The bandgap was determined by the optical method of UV–vis spectroscopy. As shown in Figure 4a, **1** displays intense light absorption with the band edge onset at 618 nm (~2.01 eV), corresponding to the dark red appearance of the crystals. The variation of absorption versus photon energy reveals the indirect bandgap (Figure 4a, inset).[43] From the *Tauc* plot, the bandgap fit to the indirect transition model is 2.03 eV that is well matched with the initial absorption photon energy of the band edge. The light
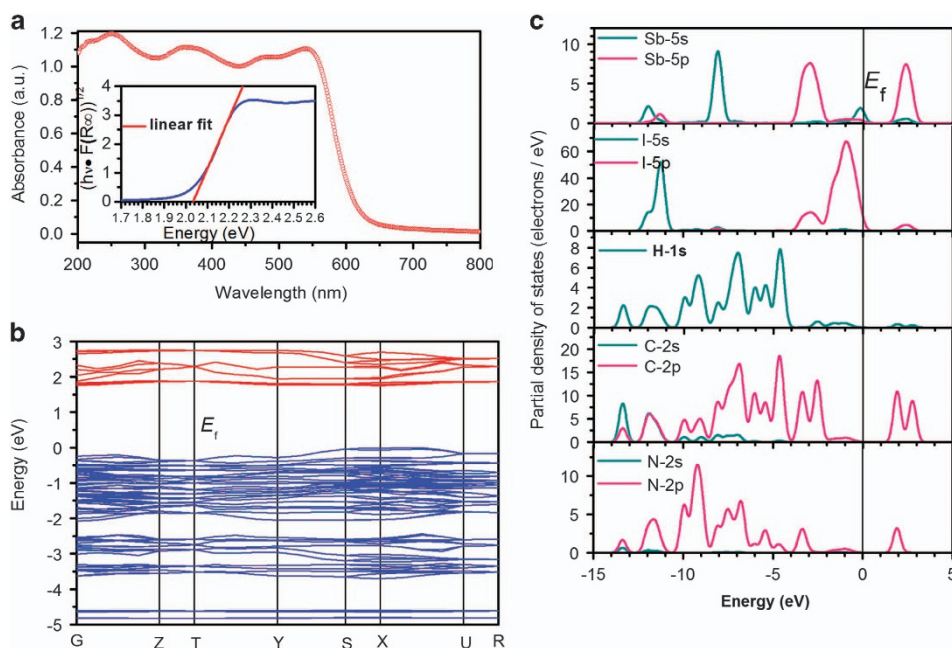
Figure 4 The electronic characteristic of **1**. (**a**) The ultraviolet–visible (UV – vis) absorption spectrum. The inset shows the *Tauc* plot with an estimated bandgap of 2.03 eV. (**b**) The energy band structure. (**c**) The partial density of states (PDOS).

absorption and bandgap are comparable to those observed for a single sheet of two-dimensional hybrid lead-iodide perovskites but weaker and larger than those for multi-sheets and for three-dimensional perovskites ($E_g \approx 1.58$ eV).[44,45] The photoluminescence spectra of the bulk crystal and the absorption spectra of the thin film were also recorded at room temperature (Supplementary Figures S11 and S12, Supplementary Information).

To gain deeper insight into the electronic structure, the band diagram of **1** (Figure 4b) was calculated based on density functional theory. The conduction band minimum and the valence band maximum are not localized at the same position in the Brillouin zone (Supplementary Figure S13), confirming that **1** is an indirect bandgap semiconductor. The calculated bandgap is 1.75 eV, slightly smaller than the experimental value of 2.03 eV. This is because of limitations of the density functional theory method. As the energy difference between the calculated direct and indirect bandgaps is small, the band structure of **1** can be considered a quasi-direct band type, corresponding to strong light absorption. In Figure 4c, the bands were assigned according to the partial density of states. The bands at the valence band top originate from the nonbonding states of I-5p, and those at the conduction band bottom are mainly from the unoccupied Sb-5p orbitals. Clearly, both the valence band maximum and the conduction band minimum are from the electronic states of Sb and I atoms, and hence it is the inorganic SbI_5 framework that determines the bandgap of the material.

CONCLUSION

In summary, we have successfully implemented above-room-temperature ferroelectricity in the semiconducting organic–inorganic hybrid material of (2-(ammoniomethyl)pyridinium)SbI₅. As a molecular ferroelectric material, in addition to showing decent ferroelectric properties, our compound displays a very small bandgap of 2.03 eV with strong absorption ability. These intriguing properties, including excellent ferroelectricity, a small bandgap, good moisture instability

and lead-free composition, suggest promising applications in the field of optoelectronics and PVs.

CONFLICT OF INTEREST

The authors declare no conflict of interest.

1 Yang, W. S., Noh, J. H., Jeon, N. J., Kim, Y. C., Ryu, S., Seo, J. & Seok, S. I. High-performance photovoltaic perovskite layers fabricated through intramolecular exchange. *Science* **348**, 1234–1237 (2015).
2 Jeon, N. J., Noh, J. H., Yang, W. S., Kim, Y. C., Ryu, S., Seo, J. & Seok, S. I. Compositional engineering of perovskite materials for high-performance solar cells. *Nature* **517**, 476–480 (2015).
3 Pellet, N., Gao, P., Gregori, G., Yang, T. Y., Nazeeruddin, M. K., Maier, J. & Gratzel, M. Mixed-organic-cation perovskite photovoltaics for enhanced solar-light harvesting. *Angew. Chem. Int. Ed.* **53**, 3151–3157 (2014).
4 Yang, B., Dyck, O., Poplawsky, J., Keum, J., Das, S., Puretzky, A., Aytug, T., Joshi, P. C., Rouleau, C. M., Duscher, G., Geohegan, D. B. & Xiao, K. Controllable growth of perovskite films by room-temperature air exposure for efficient planar heterojunction photovoltaic cells. *Angew. Chem. Int. Ed.* **54**, 14862–14865 (2015).
5 Zhou, Z., Wang, Z., Zhou, Y., Pang, S., Wang, D., Xu, H., Liu, Z., Padture, N. P. & Cui, G. Methylamine-gas-induced defect-healing behavior of ch3nh3pbi3 thin films for perovskite solar cells. *Angew. Chem. Int. Ed.* **54**, 9705–9709 (2015).
6 Green, M. A. & Bein, T. Photovoltaics perovskite cells charge forward. *Nat. Mater.* **14**, 559–561 (2015).
7 Hao, F., Stoumpos, C. C., Cao, D. H., Chang, R. P. H. & Kanatzidis, M. G. Lead-free solid-state organic–inorganic halide perovskite solar cells. *Nat. Photonics* **8**, 489–494 (2014).
8 Hao, F., Stoumpos, C. C., Guo, P. J., Zhou, N. J., Marks, T. J., Chang, R. P. H. & Kanatzidis, M. G. Solvent-mediated crystallization of CH₃NH₃SnI₃ films for heterojunction depleted perovskite solar cells. *J. Am. Chem. Soc.* **137**, 11445–11452 (2015).
9 Choi, T., Lee, S., Choi, Y. J., Kiryukhin, V. & Cheong, S. W. Switchable ferroelectric diode and photovoltaic effect in BiFeO₃. *Science* **324**, 63–66 (2009).
10 Grinberg, I., West, D. V., Torres, M., Gou, G. Y., Stein, D. M., Wu, L. Y., Chen, G. N., Gallo, E. M., Akbashev, A. R., Davies, P. K., Spanier, J. E. & Rappe, A. M. Perovskite oxides for visible-light-absorbing ferroelectric and photovoltaic materials. *Nature* **503**, 509–512 (2013).

11 Yang, S. Y., Seidel, J., Byrnes, S. J., Shafer, P., Yang, C. H., Rossell, M. D., Yu, P., Chu, Y. H., Scott, J. F., Ager, J. W. III, Martin, L. W. & Ramesh, R. Above-bandgap voltages from ferroelectric photovoltaic devices. *Nat. Nanotechnol.* **5**, 143–147 (2010).

12 Ho Sung, J., Lee, W.-M., Hong Lee, J., Chu, K., Lee, D., Moya, X., Mathur, N. D., Yang, C.-H., Park, J.-H. & Jo, M.-H. Single ferroelectric-domain photovoltaic switch based on lateral BiFeO₃ cells. *NPG Asia Mater.* **5**, e189 (2013).

13 Ye, H. Y., Liao, W. Q., Hu, C. L., Zhang, Y., You, Y. M., Mao, J. G., Li, P. F. & Xiong, R. G. Bandgap engineering of lead-halide perovskite-type ferroelectrics. *Adv. Mater.* **28**, 2579–2586 (2016).

14 Liao, W. Q., Zhang, Y., Hu, C. L., Mao, J. G., Ye, H.-Y., Li, P. F., Huang, S. D. & Xiong, R.-G. A lead-halide perovskite molecular ferroelectric semiconductor. *Nat. Commun.* **6**, 7338 (2015).

15 Park, B. W., Philippe, B., Zhang, X., Rensmo, H., Boschloo, G. & Johansson, E. M. Bismuth based hybrid perovskites A₃Bi₂I₉ (A: Methylammonium or cesium) for solar cell application. *Adv. Mater.* **27**, 6808–6813 (2015).

16 Saparov, B., Hong, F., Sun, J. P., Duan, H. S., Meng, W. W., Cameron, S., Hill, I. G., Yan, Y. F. & Mitzi, D. B. Thin-film preparation and characterization of Cs₃Sb₂I₉: a lead-free layered perovskite semiconductor. *Chem. Mater.* **27**, 5622–5632 (2015).

17 Ye, H.-Y., Li, S. H., Zhang, Y., Zhou, L., Deng, F. & Xiong, R.-G. Solid state molecular dynamic investigation of an inclusion ferroelectric: [(2,6-diisopropylanilinium)([18] crown-6)]BF₄. *J. Am. Chem. Soc.* **136**, 10033–10040 (2014).

18 Ye, H.-Y., Zhang, Y., Fu, D. W. & Xiong, R.-G. A displacive-type metal crown ether ferroelectric compound: Ca(NO₃)₂(15-crown-5). *Angew. Chem. Int. Ed.* **53**, 6724–6729 (2014).

19 Segall, M. D., Lindan, P. J. D., Probert, M. J., Pickard, C. J., Hasnip, P. J., Clark, S. J. & Payne, M. C. First-principles simulation: ideas, illustrations and the CASTEP code. *J. Phys. Condens. Matter* **14**, 2717–2744 (2002).

20 Perdew, J. P., Burke, K. & Ernzerhof, M. Generalized gradient approximation made simple. *Phys. Rev. Lett.* **77**, 3865–3868 (1996).

21 Mercier, N., Louvain, N. & Bi, W. H. Structural diversity and retro-crystal engineering analysis of iodometalate hybrids. *CrystEngComm.* **11**, 720–734 (2009).

22 Mitzi, D. B. Synthesis, structure, and properties of organic-inorganic perovskites and related materials. *Prog. Inorg. Chem.* **48**, 1–121 (1999).

23 Saparov, B. & Mitzi, D. B. Organic-inorganic perovskites: structural versatility for functional materials design. *Chem. Rev.* **116**, 4558–4596 (2016).

24 Mitzi, D. B., Feild, C. A., Harrison, W. T. A. & Guloy, A. M. Conducting tin halides with a layered organic-based perovskite structure. *Nature* **369**, 467–469 (1994).

25 Kagan, C. R., Mitzi, D. B. & Dimitrakopoulos, C. D. Organic-inorganic hybrid materials as semiconducting channels in thin-film field-effect transistors. *Science* **286**, 945–947 (1999).

26 Ishi, J., Kunugita, H., Ema, K., Ban, T. & Kondo, T. Time-to-space conversion of Tbits/s optical pulses using a self-organized quantum-well material. *Appl. Phys. Lett.* **77**, 3487–3489 (2000).

27 Stranks, S. D., Eperon, G. E., Grancini, G., Menelaou, C., Alcocer, M. J. P., Leijtens, T., Herz, L. M., Petrozza, A. & Snaith, H. J. Electron-hole diffusion lengths exceeding 1 micrometer in an organometal trihalide perovskite absorber. *Science* **342**, 341–344 (2013).

28 Wehrenfennig, C., Eperon, G. E., Johnston, M. B., Snaith, H. J. & Herz, L. M. High charge carrier mobilities and lifetimes in organolead trihalide perovskites. *Adv. Mater.* **26**, 1584–1589 (2014).

29 Lines, M. E. & Glass, A. M. *Principles and Applications of Ferroelectrics and Related Materials* (Clarendon Press: Oxford, 1977).

30 Poglitsch, A. & Weber, D. Dynamic disorder in methylammoniumtrihalogenoplumbates (II) observed by millimeter-wave spectroscopy. *J. Chem. Phys.* **87**, 6373 (1987).

31 Stoumpos, C. C., Malliakas, C. D. & Kanatzidis, M. G. Semiconducting tin and lead iodide perovskites with organic cations: phase transitions, high mobilities, and near-infrared photoluminescent properties. *Inorg. Chem.* **52**, 9019–9038 (2013).

32 Yang, T. Y., Gregori, G., Pellet, N., Gratzel, M. & Maier, J. The significance of ion conduction in a hybrid organic-inorganic lead-iodide-based perovskite photosensitizer. *Angew. Chem. Int. Ed.* **54**, 7905–7910 (2015).

33 Zhang, W., Cai, Y., Xiong, R.-G., Yoshikawa, H. & Awaga, K. Exceptional dielectric phase transitions in a perovskite-type cage compound. *Angew. Chem. Int. Ed.* **49**, 6608–6610 (2010).

34 Sawyer, C. & Tower, C. Rochelle salt as a dielectric. *Phys. Rev.* **35**, 269–273 (1930).

35 Zhang, W. & Xiong, R.-G. Ferroelectric metal-organic frameworks. *Chem. Rev.* **112**, 1163–1195 (2012).

36 Xu, G. C., Zhang, W., Ma, X. M., Chen, Y. H., Zhang, L., Cai, H. L., Wang, Z. M., Xiong, R.-G. & Gao, S. Coexistence of magnetic and electric orderings in the metal-formate frameworks of [NH₄][M(HCOO)₃]. *J. Am. Chem. Soc.* **133**, 14948–14951 (2011).

37 Ye, H.-Y., Zhang, Y., Fu, D.-W. & Xiong, R.-G. An above-room-temperature ferroelectric organo-metal halide perovskite: (3-pyrrolinium)(CdCl₃). *Angew. Chem. Int. Ed.* **53**, 11242–11247 (2014).

38 Sun, Z., Liu, X., Khan, T., Ji, C., Asghar, M. A., Zhao, S., Li, L., Hong, M. & Luo, J. A photoferroelectric perovskite-type organometallic halide with exceptional anisotropy of bulk photovoltaic effects. *Angew. Chem. Int. Ed.* **55**, 6545–6550 (2016).

39 Fu, D. W., Zhang, W., Cai, H. L., Zhang, Y., Ge, J. Z., Xiong, R.-G., Huang, S. D. & Nakamura, T. A multiferroic perdeutero metal-organic framework. *Angew. Chem. Int. Ed.* **50**, 11947–11951 (2011).

40 Li, X. L., Chen, K., Liu, Y., Wang, Z. X., Wang, T. W., Zuo, J. L., Li, Y. Z., Wang, Y., Zhu, J. S., Liu, J. M., Song, Y. & You, X. Z. Molecule-based ferroelectric thin films: mononuclear lanthanide enantiomers displaying room-temperature ferroelectric and dielectric properties. *Angew. Chem. Int. Ed.* **46**, 6820–6823 (2007).

41 Gao, W., Chang, L., Ma, H., You, L., Yin, J., Liu, J., Liu, Z., Wang, J. & Yuan, G. Flexible organic ferroelectric films with a large piezoelectric response. *NPG Asia Mater.* **7**, e189 (2015).

42 Fukunaga, M. & Noda, Y. New technique for measuring ferroelectric and antiferroelectric hysteresis loops. *J. Phys. Soc. Jpn* **77**, 064706 (2008).

43 Tauc, J., Grigorov, R & Vancu, A. Optical properties and electronic structure of amorphous germanium. *Phys. Stat. Sol. (b)* **15**, 627–637 (1966).

44 Cao, D. H., Stoumpos, C. C., Farha, O. K., Hupp, J. T. & Kanatzidis, M. G. 2D homologous perovskites as light-absorbing materials for solar cell applications. *J. Am. Chem. Soc.* **137**, 7843–7850 (2015).

45 Smith, I. C., Hoke, E. T., Solis-Ibarra, D., McGehee, M. D. & Karunadasa, H. I. A layered hybrid perovskite solar-cell absorber with enhanced moisture stability. *Angew. Chem. Int. Ed.* **53**, 11232–11235 (2014).

Supplementary Information accompanies the paper on the NPG Asia Materials website (http://www.nature.com/am)